Supplementary Information

Self-Sustained Moist-Electric Generator with Enhanced Energy Density and Longevity through a Bilayer Approach

*Jie Chen[a], Xuezhong Zhang[b,a], Minhan Cheng[a], Qianyang Li[a], Shuaijiang Zhao[a], Mao Zhang[a], Qiang Fu[a] and Hua Deng[a]**

[a]College of Polymer Science and Engineering, State Key Laboratory of Polymer Materials Engineering, Sichuan University, Chengdu 610065, P. R. China

[b]School of New Energy and Materials, Southwest Petroleum University, Chengdu 610065, P.R. China

*Corresponding author E-mail address: E-mail: huadeng@scu.edu.cn

Characterization

The morphology of GO and PGO was studied with Transmission Electron Microscope (TEM). Electrical and moisture-electrical properties were collected by Keithley 2450. Wide-angle X-ray diffraction (WAXD) was conducted on a Rigaku Ultima IV instrument at 10° min^{-1} from 5 to 60°. X-ray fluorescence spectroscopy was measured by Thermo Scientific K-Alpha. Fourier-transform infrared spectroscopy (FTIR) was measured using Thermo Scientific Nicolet iS50 FTIR Spectrometer. Raman spectra were measured by Renishaw inVia confocal Raman microscope. The Zeta potential of GO and PGO suspensions were characterized by Brookhaven Zeta PALS 190 Plus.

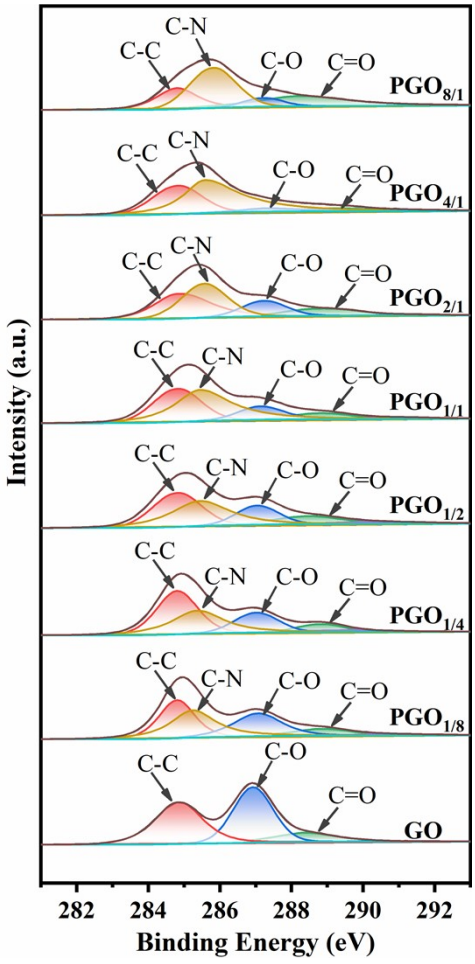

Fig. S1 XPS of C1s peak of PGO and GO

The conductivity of PGO exhibited a notable increase with the increase of Py content, reaching a value of 1.14 S/cm when the ratio between Py and GO was 8:1.

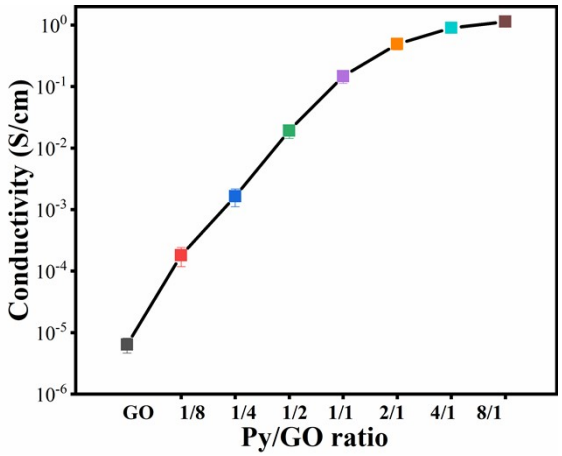

Fig. S2 Conductivity of PGO with different Py and GO ratios

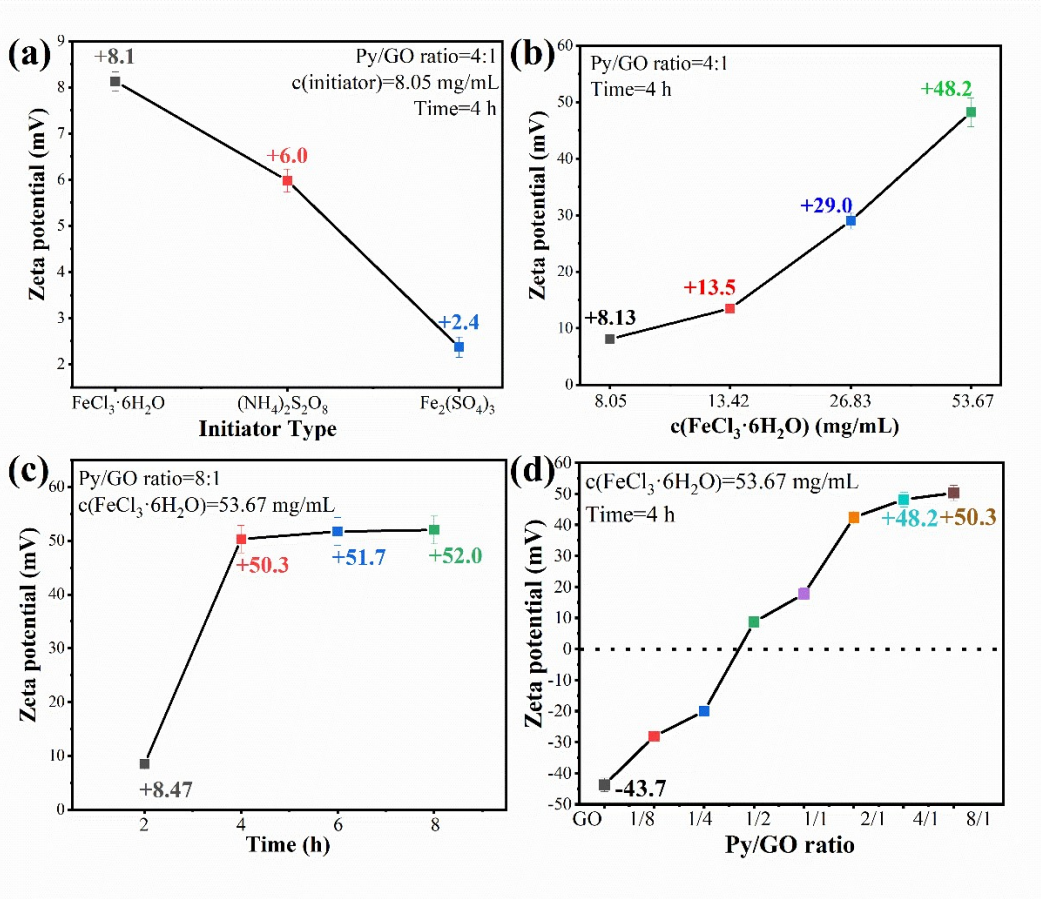

Fig. S3 Zeta potential of PGO under different synthesis conditions.(All synthesis conditions were repeated three times)

Fig. S4 illustrates that the zeta potential of PGO remains consistent across varying storage durations, thereby proving the excellent stability of PGO.

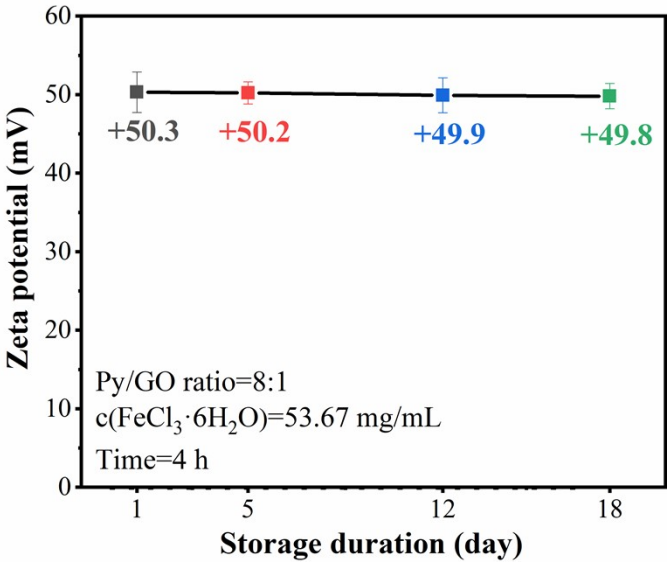

Fig. S4 Zeta potential of PGO under different storage duration

Fig. S5 Photographs of PGO (Left) and GO (Right)

Schematic diagram of the structure

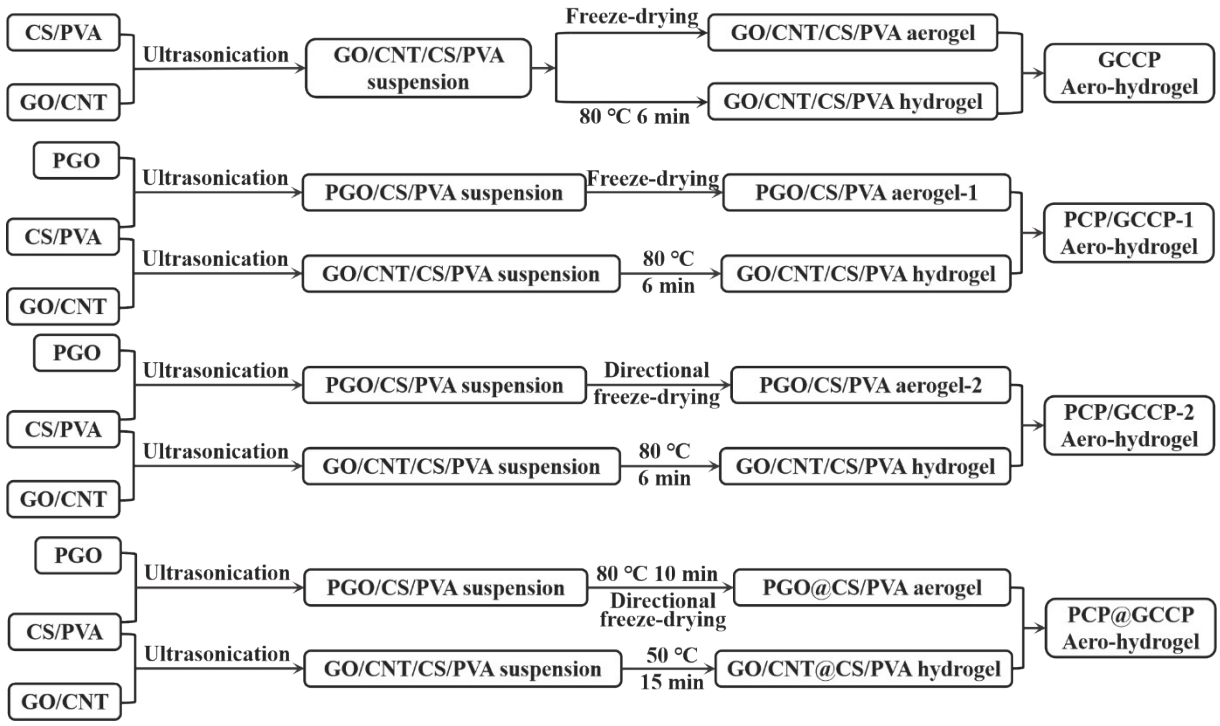

Fig. S6 Diagram of PCP@GCCP aero-hydrogel fabrication process

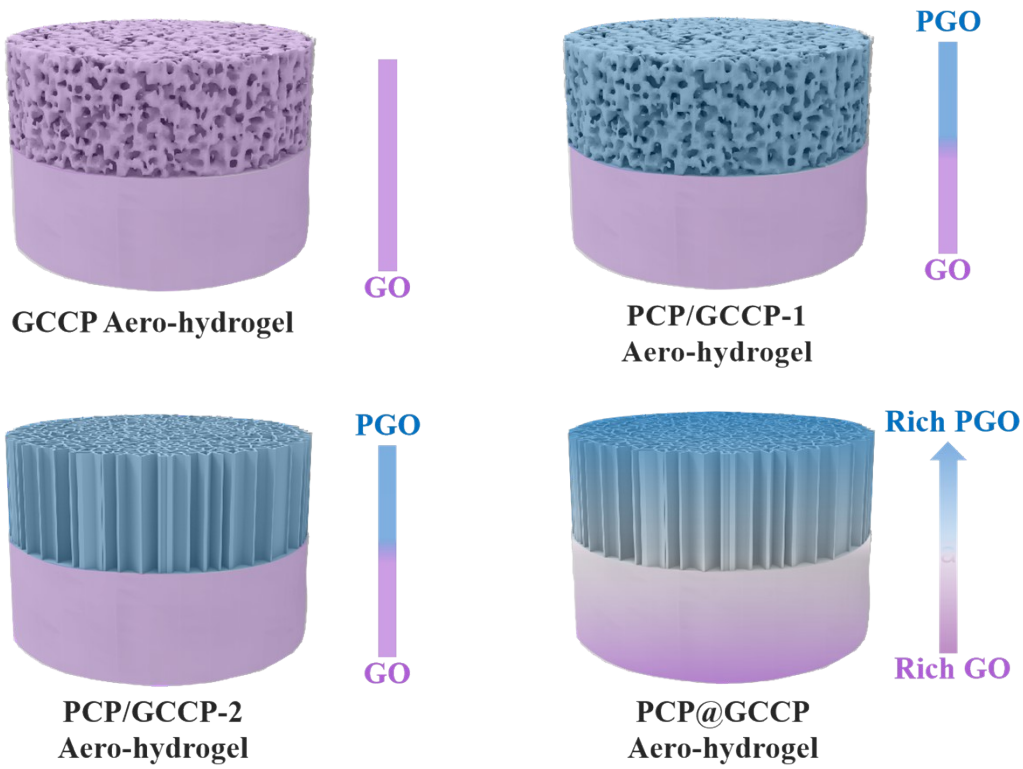

Fig. S7 Schematic diagram of four different aero-hydrogels

Calculation of filler content in different regions of the PCP@GCCP

The filler content in the various areas was calculated by carbon residue in the other regions. The residual carbon contents of CS/PVA, PGO, and GO/CNT are denoted as M_0, M_1, and M_2, respectively. The residual carbon contents in the Low-PGO, Rich-PGO, Rich-GO/CNT, and Low-GO/CNT regions of the PCP@GCCP are represented by *M3*, *M4*, *M5*, and *M6*, respectively. The filler contents in the Low-PGO, Rich-PGO, Rich-GO/CNT, and Low-GO/CNT regions are denoted as $\varphi 1$, $\varphi 2$, $\varphi 3$, and $\varphi 4$, respectively. The filler content is calculated as follows:

$$M_3 = \varphi_1 \times M_1 + (100 - \varphi_1) \times M_0 \quad (1)$$

$$M_4 = \varphi_2 \times M_1 + (100 - \varphi_2) \times M_0 \quad (2)$$

$$M_5 = \varphi_3 \times M_2 + (100 - \varphi_3) \times M_0 \quad (3)$$

$$M_6 = \varphi_4 \times M_2 + (100 - \varphi_4) \times M_0 \quad (4)$$

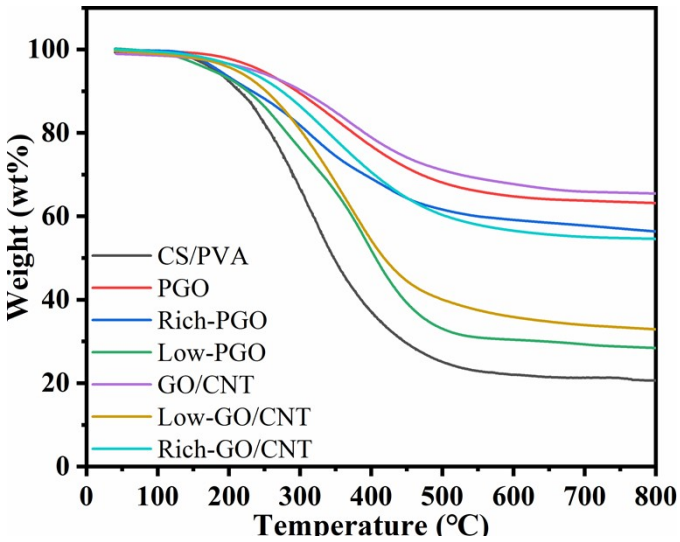

Fig. S8 TGA of CS/PVA and the PCP@GCCP

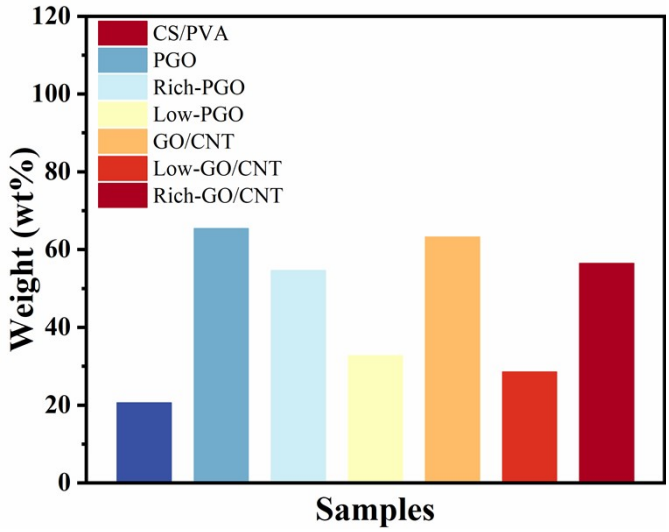

Fig. S9 Residual carbon rate of CS/PVA and the PCP@GCCP

Table S1. The filler contents in different regions of the PCP@GCCP

Samples	Residual carbon rate (wt%)	Filler content (wt%)
PVA/CS	20.6	-
PGO	65.4	-
Rich PGO	54.6	76
Low PGO	32.7	27
GO/CNT	63.2	-
Low GO/CNT	28.5	20
Rich GO/CNT	56.4	84

Moist-electric generators (MEGs)

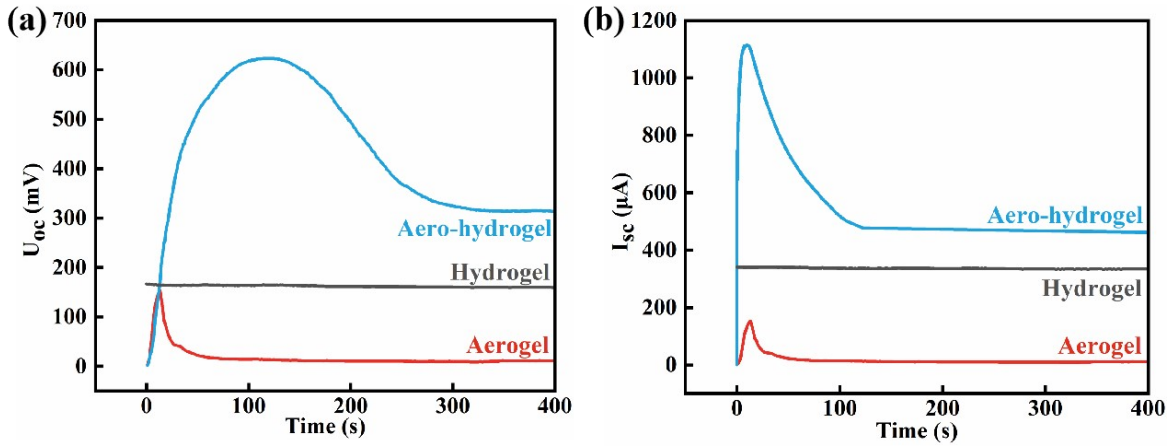

Fig. S10 Comparison of moist-electric properties of typical aerogel and hydrogel with PCP@GCCP aero-hydrogel

GO and PGO are capable of constructing extensive ion density gradients in the upper and lower layers(-43.7 ~ +50.3 mV). CNT, despite exhibiting a comparatively lower absolute value of zeta potential than GO, is able to markedly enhance the conductivity of the hydrogel. The combined advantages of both are mutually reinforcing.

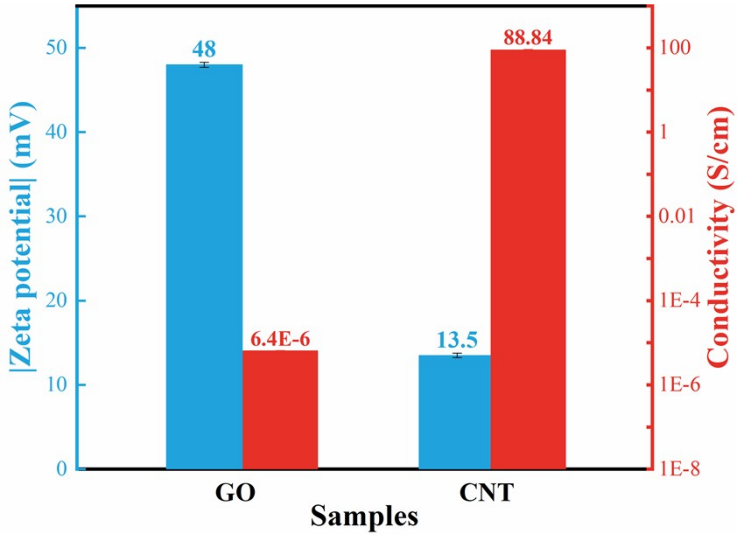

Fig. S11 Comparison of GO and CNT with zeta potential and conductivity

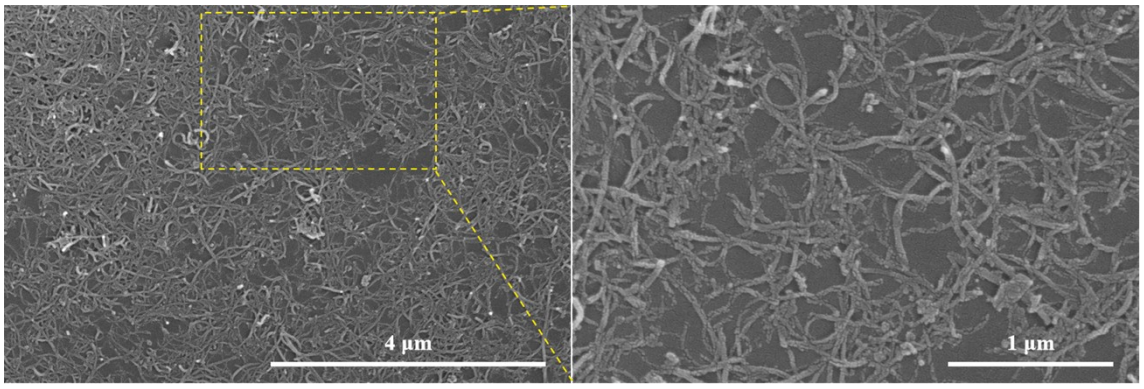

Fig. S12 SEM image of the CNT filler

As illustrated in Fig. S13a, both open-circuit voltage and short-circuit current initially increase with aerogel thickness, reaching a maximum at 10 mm, after which they decrease. This behavior is attributed to the series-like effect of increasing aerogel thickness, which enhances open-circuit voltage. Meanwhile, the short-circuit current increases with higher hydrogel moisture content. However, when the aerogel thickness exceeds a certain point, its water absorption capacity decreases due to gravity's effect on moisture transport, leading to a reduction in performance. This relationship is a balancing act between these competing factors. Fig. S13b demonstrates that both the open-circuit voltage and short-circuit current increase with hydrogel thickness. However, maintaining a balance between moisture absorption and evaporation is crucial. Excess moisture during long-term operation can hinder optimal performance.

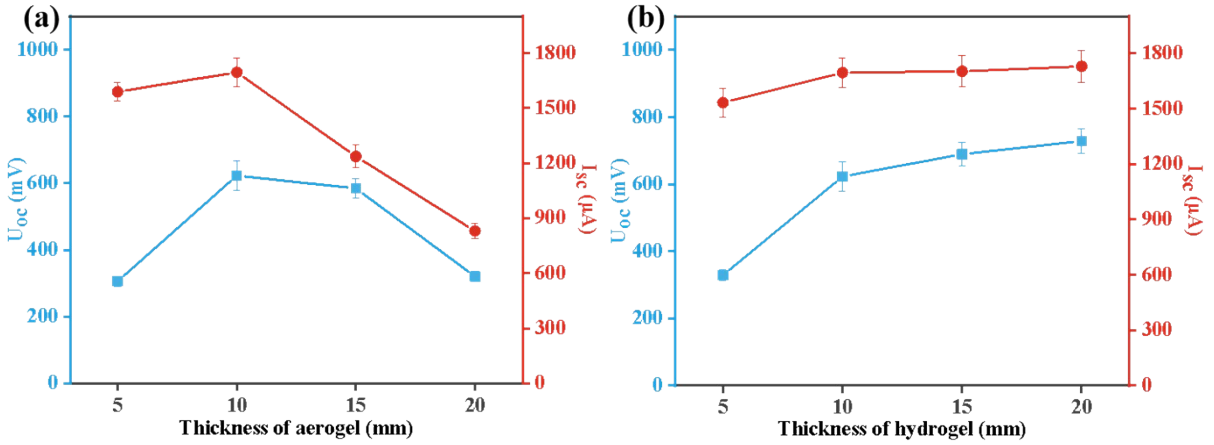

Fig. S13 U_{oc} and I_{sc} with different thickness of aerogel and hydrogel

Calculation of internal energy conversion efficiency.

The energy density output (EMEGs) of MEGs can be calculated as: $EMEGs = \frac{\int Isc(t) \times Uoc(t) d(t)}{S}$ where $Isc(t)$, $Uoc(t)$, t and S is the short-circuit current, open-circuit voltage, the complete cycle time and the cross-sectional area. The calculation results showed ca. 809.2 μW·h·cm^{-2}.

Table S2. Comparison of MEGs in this work with literature

Active material	Matrix	Structure	Methodology	Ion gradient	Power density (μw·cm^{-2})	Energy density (μw·h·cm^{-2})	Ref
GO	PVA	Aerogel	Freeze-drying	Yes	22.95	7.73	[24]
PEDOT:PSS	PSSA	Aerogel	Freeze-drying	Yes	26.55	81.79	[25]
GO	PU	Foam	Coating	Yes	65.97	225.4	[26]
IL-GO/GO	PVA	Aerogel	Freeze-dring	Yes	22.55	75.16	[27]
SWNT	PVA/CS/CNF	Aerogel	Freeze-dring	Yes	11.32	165.23	[30]
CB	PVA	Hydrogel	Cross-linking	No	15.03	45.08	[32]
CNT/TiO_2	PVDF/PU	Foam	Coating	No	8.01	5.82	[44]
Phytic acid	PVA	Hydrogel	Cross-linking	Yes	35	15.73	[51]
MOF/GO	ILs	Film	Cast forming	Yes	12	31.45	[52]
Protein nanofibrils		Film	Coating	No	9.02	7.55	[53]
Cellulose/SDBS		Fabric	Electrospining	Yes	11.5	24.22	[54]
CNTs	Cellulose	Paper	Coating	No	14	3.37	[55]
TiO_2	poly(ethylene terephthalate)	Film	Electrophoretic deposition	No	4	0.8	[56]
PGO/GO	CS/PVA	Aero-hydrogel	Freeze-dring	Yes	20.7	809.2	Our work

Figure 4a illustrates the top cross-section while Figure 4b and 4c depict the front side cross section and side cross-section of the PGO@CS/PVA aerogel, demonstrating the successful construction of a vertically oriented structure.The pore channels of the unoriented PGO/CS/PVA aerogel-1 are not oriented in a single direction in comparison to the vertically oriented PGO@CS/PVA aerogel. The freezing process occurs in a refrigerator, resulting in the generation of ice crystals from the exterior to the interior. This is evidenced by the pore channels observed in Figure S11, and the pore channels tend to cluster towards the centre of the aerogel, which impedes the transport of moisture.

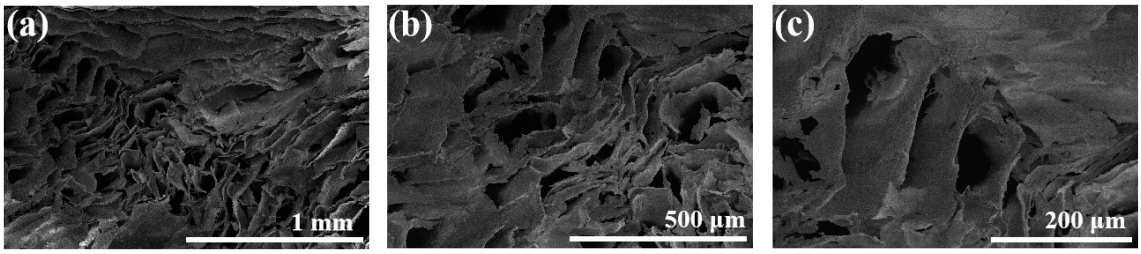

Fig. S14 FESEM of PGO/CS/PVA aerogel-1

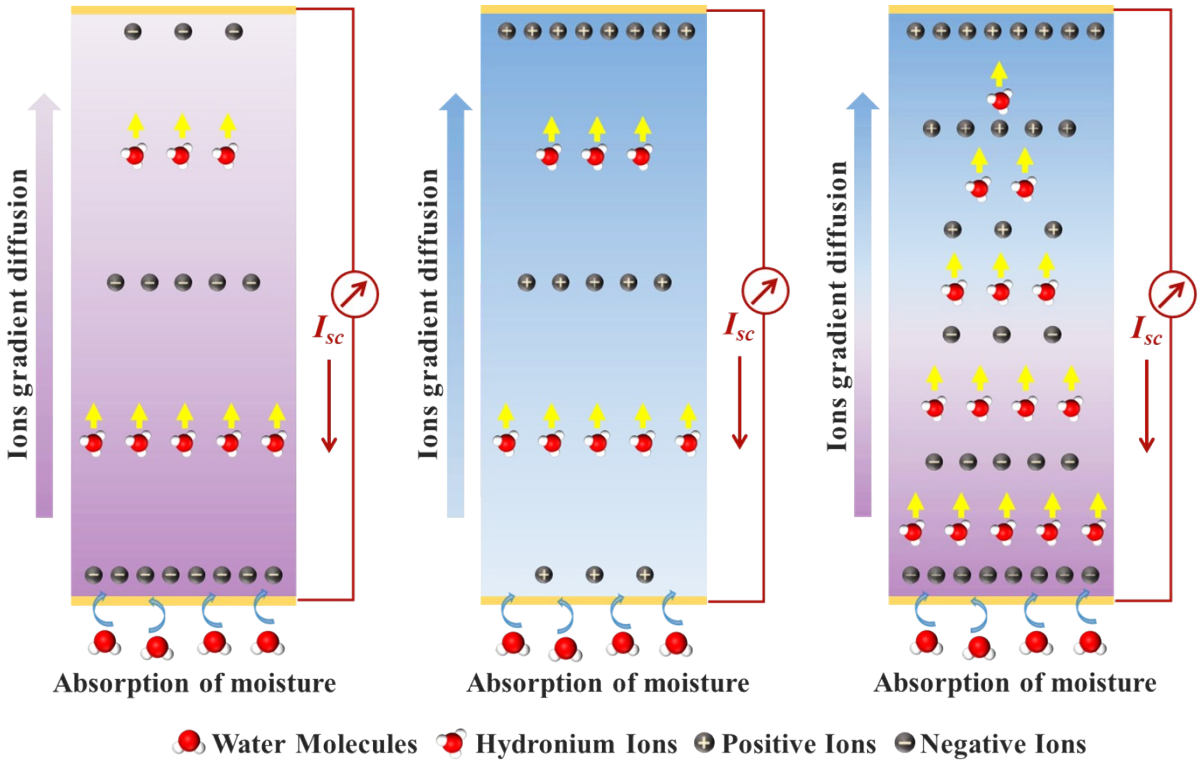

Fig. S15 Schematic diagram of the mosit-electric mechanism for PCP@GCCP aero-hydrogel.

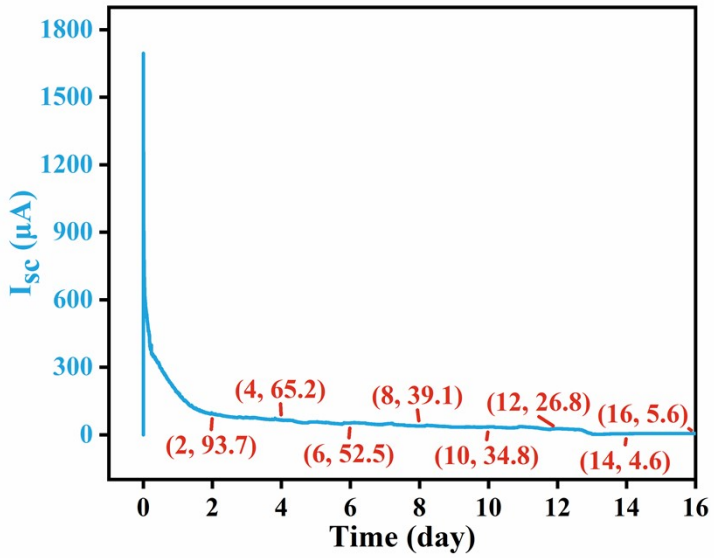

Fig. S16 Short-circuit current output of PCP@GCCP Aero-hydrogel lasting 16 days

The water contact angle of the aerogel is approximately 72 degrees, and the hydrogel displays excellent wettability. As the aerogel is not hydrophobic, although it absorbs water slowly, the evaporation of water will be slower and slower with the increase of power generation time, which ultimately results in a decrease in performance.

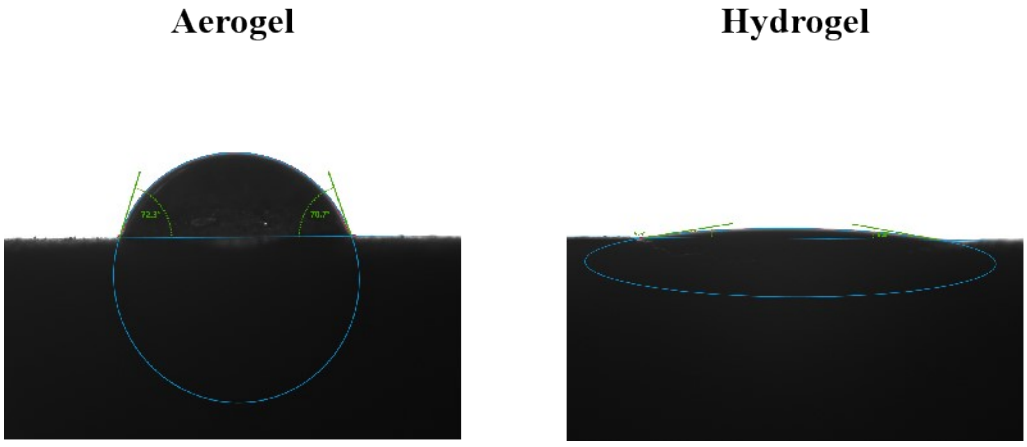

Fig. S17 Contact angle between upper aerogel and lower hydrogel layers.

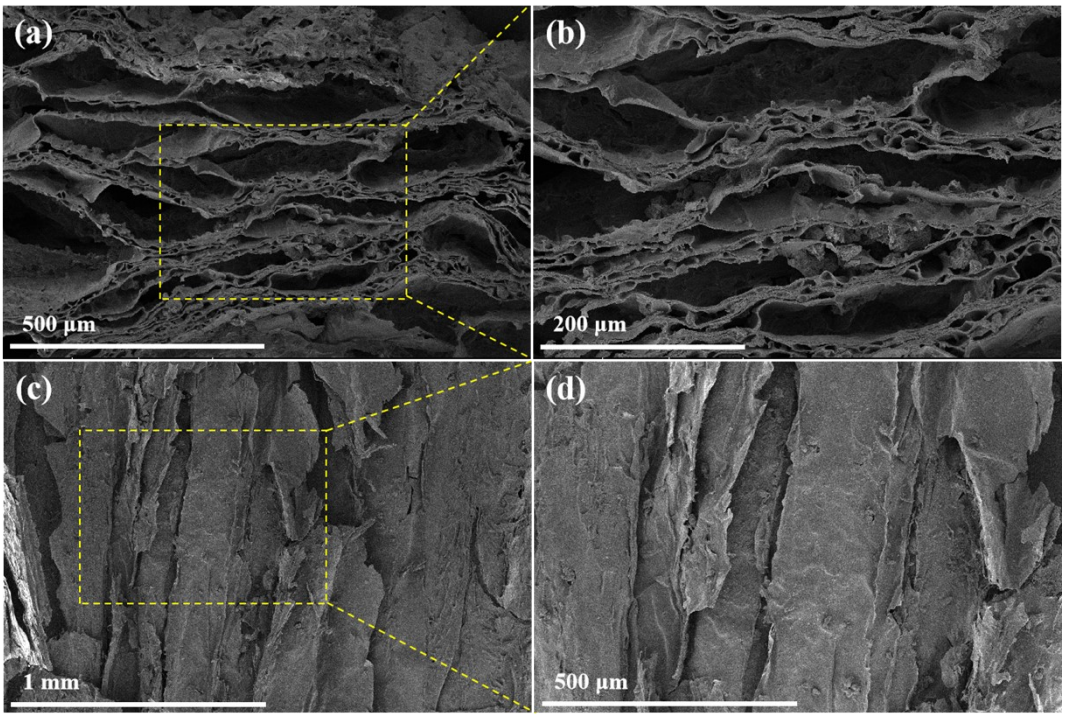

Fig. S18 SEM images (a,b) the top cross-section; (c,d) side cross-section of PCP@GCCP after 16d power generation

Table S3. the resistance and ionic conductivity of PCP@GCCP with different sustained power generation times

Duration of power generation	Resistance (Ω)	σ (mS/cm)
10 min	8.6	30.3
1 d	220	1.35
3 d	1401	0.22
16 d	14593.8	0.02

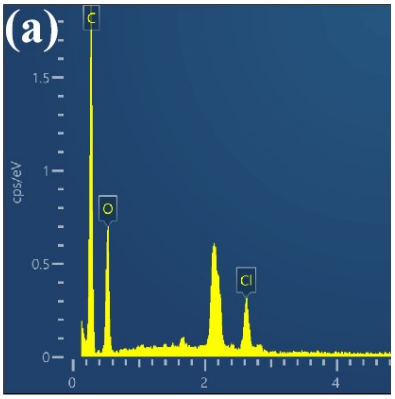

Element	Wt%	Wt% Sigma
C	66.15	0.82
O	29.62	0.81
Cl	4.22	0.19
Total	100.00	

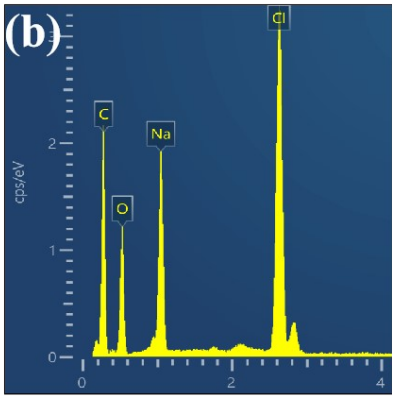

Element	Wt%	Wt% Sigma
C	56.65	0.53
O	16.76	0.38
Na	7.52	0.15
Cl	19.07	0.27
Total	100.00	

Fig. S19 EDS analysis of a PGO@CS/PVA aerogel (a) before water absorption and (b) after water absorption during moisture-driven power generation.

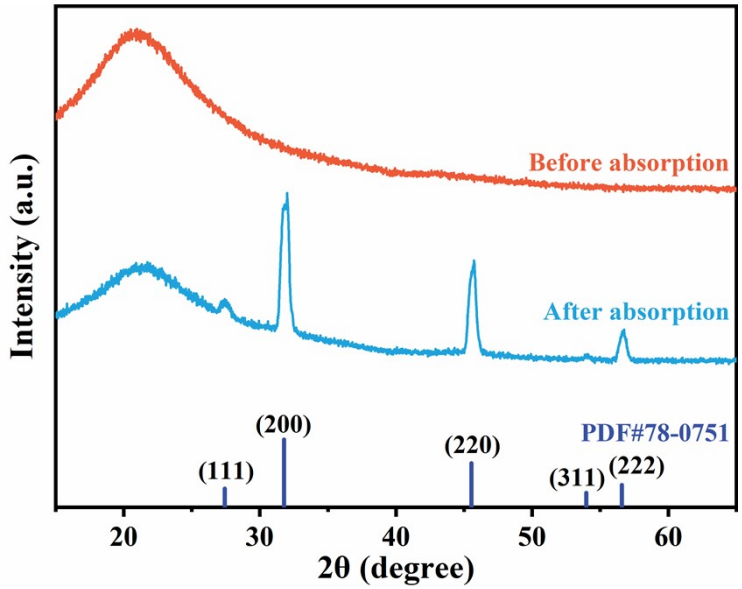

Fig. S20 XRD of a PGO@CS/PVA aerogel (a) before water absorption and (b) after water absorption during moisture-driven power generation.

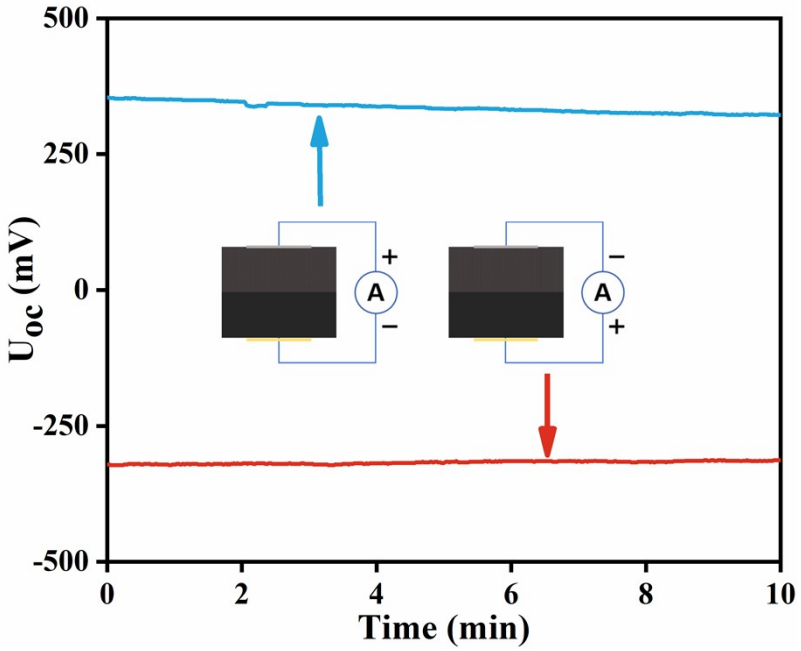

Fig. S21 Polarity test of the PCP@GCCP aero-hydrogel. Upon reversing the source-meter electrodes, the sign of the induced voltage is reversed.